

Multi-Resolution Training-Enhanced Kolmogorov-Arnold Networks for Multi-Scale PDE Problems

Yu-Sen Yang¹, Ling Guo², Xiaodan Ren^{1*}

^{1*}College of Civil Engineering, Tongji University, 1239 Siping Road,
Shanghai, 200092, China.

²Department of Mathematics, Shanghai Normal University, 100 Guilin
Road, Shanghai, 200234, China.

*Corresponding author(s). E-mail(s): rxdtj@tongji.edu.cn;
Contributing authors: 2210031@tongji.edu.cn; lguo@shnu.edu.cn;

Abstract

Multi-scale PDE problems present significant challenges in scientific computing. While conventional MLP-based deep learning methods exhibit spectral bias in resolving multi-scale features, the physics-informed Kolmogorov-Arnold network (PIKAN) mitigates this issue through its novel architecture, demonstrating certain advantages. On the other hand, insights from the information bottleneck theory suggest that high-resolution training points are essential for these hybrid methods to accurately capture multi-scale behavior, although this requirement often leads to longer training times. To address this challenge, we propose a simple yet effective multi-resolution training-enhanced PIKAN framework, termed MR-PIKAN, which trains the data-physics hybrid model either sequentially or alternately across different resolutions. The proposed MR-PIKAN is validated on various multi-scale forward and inverse PDE problems. Numerical results indicate that this new training strategy effectively reduces computational costs without sacrificing accuracy, thereby enabling efficient solutions of complex multi-scale PDEs in both forward and inverse settings.

Keywords: Multi-resolution training, Kolmogorov-Arnold Networks, Hybrid modeling methods, Multi-scale modeling

Article Highlights

- Through information bottleneck analysis, we empirically demonstrate that sampling resolution is a critical factor for multi-scale physical modeling using the hybrid physics-informed machine learning methods.
- A simple but effective multi-resolution training method for PIKAN is proposed, where the model is trained sequentially or alternately at different resolutions.
- The proposed MR-PIKAN model is validated on various multi-scale forward and inverse PDE problems, demonstrating significant reductions in computational cost while maintaining solution accuracy.

1 Introduction

Multi-scale PDE problems are fundamental in engineering and scientific computing, yet capturing multi-scale features presents significant computational challenges. Recently, physics-informed machine learning, a novel computational approach that integrates data with physical knowledge, has gained widespread attention and demonstrated unique advantages in solving high-dimensional, multi-scale, and inverse problems. The earlier works include the neural network-based differential equation solver [1, 2], the Deep Ritz Method [3], the physics-informed neural networks (PINNs) [4–6], Variational PINN [7], and the Deep Energy Method [8].

Despite their strong approximation capabilities [9], deep neural networks face training challenges when modeling physical systems involving high-frequency or multi-scale behavior [10, 11]. The challenges of PINN-based methods can be broadly categorized into two main aspects. First, neural networks often struggle to effectively capture high-frequency components in physical fields or signals. Second, multi-scale physical systems require a significantly large number of sampling points for training, resulting in substantial computational burdens.

The analysis of [10, 11] revealed that MLPs exhibit significantly slower convergence for high-frequency components, highlighting the spectral bias pathology. Therefore, researchers have proposed adaptive activation functions, input variable scaling and Fourier feature mapping based on the vanilla MLP architecture to address this issue [11–14]. As an alternative to MLP, researchers have recently proposed Kolmogorov-Arnold Networks (KANs) [15, 16]. Various KAN variants have been developed through different approximations of the nonlinear univariate activation functions [17–20]. As reported in [21], physics-informed KAN (PIKAN) exhibits reduced spectral bias compared to MLPs and offers certain advantages in modeling multi-scale problems.

Although improvements of the MLP and the emergence of the KAN have alleviated the challenges of expressing multi-scale physical fields, the models still require sufficient training points to capture the multi-scale features, limiting the further development of such methods. Adaptive sampling algorithms [22–26] can mitigate the aforementioned challenges. The Residual-based Adaptive Resampling (RAR) method [22, 26] allocates more sampling points in regions with larger residuals. This approach was refined by incorporating residual distribution information, balancing sampling points between large and small residual regions [24, 25, 27]. Some researchers have also used neural

networks to learn optimal sampling strategies [28]. While these methods improve solution accuracy, they introduce additional computational overhead, further increasing the training burden of physics-informed machine learning models.

An alternative approach is to decompose and solve the multi-scale problem, thereby reducing the sampling requirements at each individual scale. Several multi-scale frameworks have been proposed [29–31], where auxiliary networks are trained to learn the residuals or higher-order expanded terms of the equation, introducing additional complexity in solving nonlinear PDEs. In the computer vision field, where large datasets are common in training video models, Wu et al. [32] introduced a multigrid method to accelerate training by alternating between spatial-temporal resolutions. A similar strategy has also been applied to super-resolution video models [33], where multi-resolution data is leveraged to improve the training efficiency and performance of one single model.

To address the high-resolution sampling demands of multi-scale physical problems, we introduce a multi-resolution training strategy within the physics-informed machine learning framework. we propose the multi-resolution training-enhanced PIKAN framework, termed MR-PIKAN, for solving multi-scale forward and inverse problems. Our main contributions can be summarized as the following points:

- We analyze the training dynamics of PIKAN models under various single-resolution training settings from the perspective of information bottleneck theory. The results validate the empirical insight that higher-resolution sampling tends to be crucial for achieving accurate solutions in multi-scale physical systems.
- We introduce a simple but effective multi-resolution training strategy within the framework of PIKAN, termed MR-PIKAN, where training at lower resolutions effectively reduces the overall training time.
- The proposed MR-PIKAN model was tested on a series of multi-scale forward and inverse problems, the results indicate that the MR-PIKAN model can effectively enhance computational efficiency without compromising accuracy.

The rest of this paper is organized as follows. In Section 2, we present a brief overview of physics-informed machine learning formulation. Subsequently, the multi-resolution training method is proposed in Section 3, and the MR-PIKAN framework is introduced in detail. Next, several numerical examples are tested to demonstrate the accuracy and efficiency of the proposed MR-PIKAN in Section 4. Finally, we discuss our results and provide a summary in Section 5.

2 Physics-informed machine learning

2.1 Physics-informed machine learning framework

In this section, we present a brief overview of physics-informed machine learning (PIML) framework for solving PDE problems [4–6]. We consider the following partial differential equation:

$$\begin{cases} \mathcal{D}[\mathbf{u}](\mathbf{x}) = \mathbf{f}(\mathbf{x}) & \text{in } \Omega \\ \mathcal{B}[\mathbf{u}](\mathbf{x}) = \mathbf{0} & \text{on } \partial\Omega \end{cases} \quad (1)$$

where $\mathcal{D}[\cdot]$ represents the differential operator acting in the problem domain Ω and $\mathbf{f}(\mathbf{x})$ denotes the source term. $\mathcal{B}[\cdot]$ represents the boundary operator and $\partial\Omega$ denotes the boundary of the problem domain Ω . The basic idea of PIML is to approximate the solution of Equ. (1) using a representation model $\mathbf{u}_\theta(\mathbf{x})$, where θ denotes its trainable parameters. Then, the optimal parameters θ' can be obtained by minimizing the physics-informed *loss function*:

$$\mathcal{L}(\theta) = \omega_r \mathcal{L}_r(\theta) + \omega_b \mathcal{L}_b(\theta) \quad (2)$$

where

$$\begin{aligned} \mathcal{L}_r(\theta) &= \frac{1}{N_r} \sum_{i=1}^{N_r} |\mathcal{D}[\mathbf{u}_\theta](\mathbf{x}_r^i) - \mathbf{f}(\mathbf{x}_r^i)|^2 \\ \mathcal{L}_b(\theta) &= \frac{1}{N_b} \sum_{i=1}^{N_b} |\mathcal{B}[\mathbf{u}_\theta](\mathbf{x}_b^i)|^2 \end{aligned} \quad (3)$$

representing the loss terms associated with the governing equation and the boundary conditions, respectively. N_r and N_b denote the sizes of the training data \mathbf{x}_r^i and \mathbf{x}_b^i , respectively. The weight coefficients ω_r and ω_b are used to balance the different terms in the loss function, which can be user-specified or automatically tuned during training [34–37].

2.2 Physics-informed neural networks

When the representation model is defined using a multi-layer perceptron (MLP), the PIML formulation is referred to as physics-informed neural networks (PINNs). As shown in Fig. 1(a), an MLP consists of an input layer Φ_0 , several hidden layers $\Phi_1 \dots \Phi_L$, and an output layer \mathcal{G} , where each neuron is connected to every neuron in its adjacent layers. Considering an MLP with L hidden layers, the nonlinear

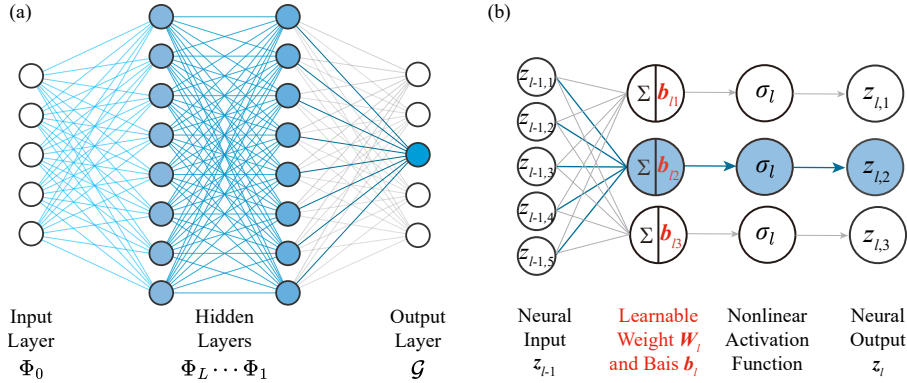


Fig. 1: Multi-Layer Perceptron (MLP): **a** Architecture of Multi-layer perceptron; **b** Operation in the l -th hidden layer of an MLP, where the weight matrix \mathbf{W}_l and bias vector \mathbf{b}_l are learnable parameters

transformation can be expressed in the following recursive form:

$$\mathbf{u}_\theta(\mathbf{x}) = \text{MLP}(\mathbf{x}) = \mathcal{G} \circ \Phi_L \circ \dots \circ \Phi_1 \circ \Phi_0(\mathbf{x}) \quad (4)$$

For the l -th hidden layer, there are N_l neurons with the activation function σ_l . Thus, as illustrated in Fig. 1(b), the transformation $\Phi_l(\cdot)$ takes the form:

$$\mathbf{z}_l = \Phi_l(\mathbf{z}_{l-1}) = \sigma_l(\mathbf{W}_l \mathbf{z}_{l-1} + \mathbf{b}_l) \text{ for } l \in [1, L] \quad (5)$$

where $\mathbf{z}_l = \{z_{l,1}, \dots, z_{l,N_l}\}$ are the neural outputs of layer l . $\mathbf{W}_l \in \mathbb{R}^{N_l \times N_{l-1}}$ and $\mathbf{b}_l \in \mathbb{R}^{N_l}$ are the learnable weight matrix and bias vector of the l -th hidden layer, respectively. For the input layer $\Phi_0(\cdot)$, we have

$$\Phi_0(\mathbf{x}) = \mathbf{x} \in \mathbb{R}^{d_{\text{in}}} \quad (6)$$

where $N_0 = d_{\text{in}}$ neurons are defined to match the dimension of the problem input. For the output layer $\mathcal{G}(\cdot)$, linear mapping is typically adopted to match the dimension of the problem output. Thus, we have

$$\mathcal{G}(\mathbf{z}_L) = \mathbf{W}_{L+1} \mathbf{z}_L + \mathbf{b}_{L+1} \quad (7)$$

The trainable parameters in the neural network $\text{MLP}(\mathbf{x})$ are $\theta = \{\mathbf{W}_l, \mathbf{b}_l \mid l = 1, \dots, L+1\}$. Due to the nonlinear activation function σ_l , the relationship between the neural network output function $\mathbf{u}(\mathbf{x})$ and the input variable \mathbf{x} is highly nonlinear.

2.3 Physics-informed Kolmogorov-Arnold networks

Inspired by the Kolmogorov-Arnold representation theorem [38], Kolmogorov-Arnold Networks (KANs) have been proposed as promising alternatives to MLPs [15]. Consequently, physics-informed Kolmogorov-Arnold networks (PIKANs) [17, 21] are introduced where the representation model is defined by a Kolmogorov-Arnold Network (KAN). Recently, Liu et al. [15] proposed a generalized version of KAN with arbitrary widths and depths, as illustrated in Fig. 2(a). Consider a KAN with L KAN layers, the nonlinear transformation can be expressed in the following recursive form:

$$\mathbf{u}_\theta(\mathbf{x}) = \text{KAN}(\mathbf{x}) = \mathcal{G} \circ \Phi_L \circ \dots \circ \Phi_1 \circ \Phi_0(\mathbf{x}) \quad (8)$$

where Φ_l represents the nonlinear transformation of the l -th KAN layer. The input layer $\Phi_0(\cdot)$ and output layer $\mathcal{G}(\cdot)$ in KAN are typically simplified to an identity mapping. In the l -th KAN layer, there are $N_l \times N_{l-1}$ univariate activation functions $\phi_{l,i_l,i_{l-1}}(\cdot)$. Therefore, the transformation $\Phi_l(\mathbf{x})$ of a KAN layer, as shown in Fig. 2(b),

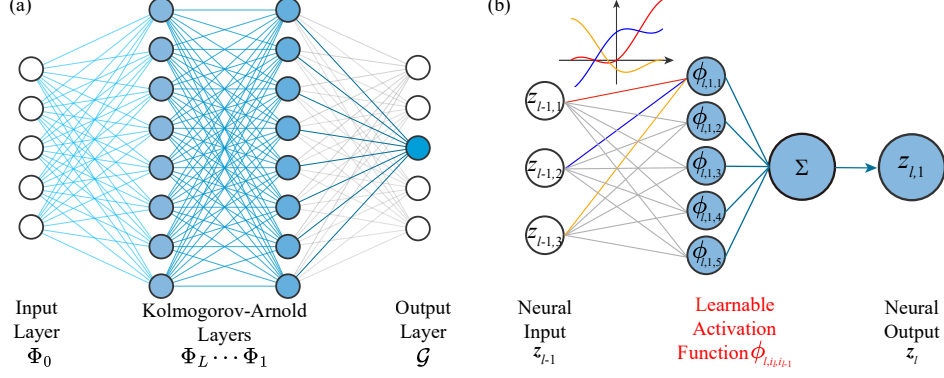


Fig. 2: Kolmogorov-Arnold Network (KAN): **a** Architecture of Kolmogorov-Arnold Network; **b** Operation of a KAN layer, where the univariate nonlinear activation functions $\phi_{l,i_l,i_{l-1}}$ are learnable

can be written as a function matrix:

$$\mathbf{z}_l = \Phi_l(\mathbf{z}_{l-1}) = \begin{bmatrix} \phi_{l,1,1}(\cdot) & \phi_{l,1,2}(\cdot) & \cdots & \phi_{l,1,N_{l-1}}(\cdot) \\ \phi_{l,2,1}(\cdot) & \phi_{l,2,2}(\cdot) & \cdots & \phi_{l,2,N_{l-1}}(\cdot) \\ \vdots & \vdots & \ddots & \vdots \\ \phi_{l,N_l,1}(\cdot) & \phi_{l,N_l,2}(\cdot) & \cdots & \phi_{l,N_l,N_{l-1}}(\cdot) \end{bmatrix} \begin{bmatrix} z_{l-1,1} \\ z_{l-1,2} \\ \vdots \\ z_{l-1,N_{l-1}} \end{bmatrix} \quad (9)$$

where $\mathbf{z}_l = \{z_{l,1}, \dots, z_{l,N_l}\}$ are the neural outputs of layer l . $\phi_{l,i_l,i_{l-1}}$ represents the learnable univariate activation function corresponding to the i_l -th feature of \mathbf{z}_l and the i_{l-1} -th feature in \mathbf{z}_{l-1} . The specific form of each $\phi(x)$ defines the variations among different KAN architectures. In the original KAN paper [15], $\phi(x)$ is defined as a weighted combination of a basis function $b(x)$ and B-splines. In particular:

$$\begin{aligned} \phi(x) &= \omega_b b(x) + \omega_s \text{spline}(x) \\ b(x) &= \text{silu}(x) = \frac{x}{1 + e^{-x}} \\ \text{spline}(x) &= \sum_i c_i B_i(x) \end{aligned} \quad (10)$$

where ω_b, ω_s and c_i are trainable parameters.

Many variations of the KAN model have emerged, such as radial basis function KANs [19], Wavelet KANs [20] and Jacobi KANs [18]. The KAN model using Chebyshev polynomials, which are a special case of Jacobi polynomials, as activation functions are reported to be more efficient than the vanilla KAN model [18]. For Chebyshev KAN, $\phi(x)$ is defined as a weighted linear combination of Chebyshev polynomials up to degree n , and the input x is normalized to the range $[-1, 1]$ using a

hyperbolic tangent function:

$$\begin{aligned}\phi(x) &= \sum_{k=0}^n \Theta_k T_k(\tilde{x}) \\ \tilde{x} &= \tanh(x)\end{aligned}\tag{11}$$

where Θ_k are the learnable coefficients for the Chebyshev interpolation. The Chebyshev polynomials of the first kind $T_n(x)$ are orthogonal with respect to the weight function $\frac{1}{\sqrt{1-x^2}}$, which can be expressed in explicit form:

$$T_n(x) = \cos(n \arccos(x))\tag{12}$$

For this Chebyshev KAN, there is no need to recursively compute the values of the Chebyshev polynomials during each forward pass, which further enhances its computational efficiency. As reported in [21], KAN exhibits a reduced spectral bias compared to MLP, which offers certain advantages in modeling multi-scale problems. Therefore, in this paper, we focus on using PIKAN models based on the Chebyshev KAN representation to solve multi-scale physical problems.

3 Multi-resolution training method

After selecting an effective neural network representation, the PIML model is trained by solving an optimization problem that allows the representation model to approximate the solution of the governing equation. Training a PIML model involves minimizing the loss function \mathcal{L} which quantifies the disagreement between the solution approximated by the representation model and the real solution of the physical system. To enable computation, the loss function \mathcal{L} is approximated over N_r residual points sampled from the domain Ω and N_b boundary points sampled from $\partial\Omega$.

As shown in Fig. 3, the residual points can either be sampled once throughout the entire training process or sampled individually at each iteration, leading to full-batch sampling and mini-batch sampling, respectively. Regardless of the batch sampling strategy used, sufficiently dense sampling is necessary to effectively capture the multi-scale features of the system [30]. To the best of the authors' knowledge, the batch size of PIML models in previous studies typically remains fixed throughout the entire training process. Therefore, we refer to this sampling method with a fixed batch size as the single-resolution (SR) training strategy.

3.1 Single-resolution training dynamics

The batch size of SR training strategy has a significant impact on the accuracy of results, with this effect becoming increasingly pronounced when solving multi-scale physical problems. Recently, the information bottleneck (IB) principle has been employed to analyze the training dynamics of PIML models. Before presenting our proposed methods, we first analyze the accuracy and training dynamics of a forward problem with multi-scale features under different single-resolution settings.

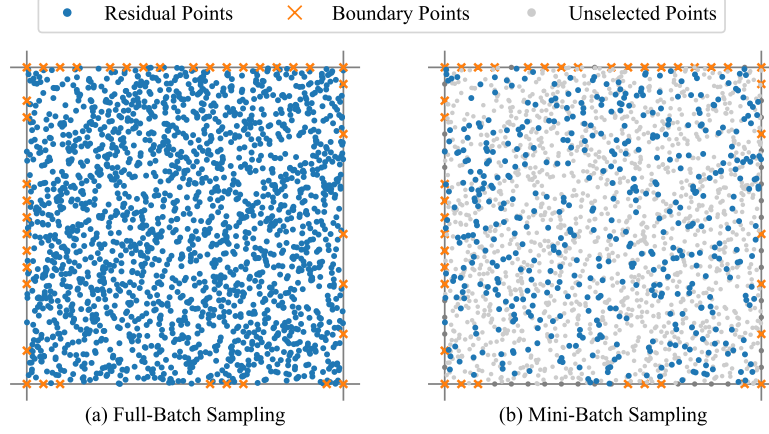


Fig. 3: Two sampling strategies for residual points in a computational domain: **a** Full-Batch Sampling: a large number of identical residual points (blue dots) are used in each iteration, ensuring accuracy at the expense of computational efficiency; **b** Mini-Batch Sampling: a variable subset of residual points (blue dots) is randomly selected in each iteration, while the unselected points (grey dots) are temporarily ignored. This reduces computational cost but may introduce noise into the solution process. A small number of boundary points (orange crosses) are typically utilized in their entirety during the gradient computation process

Consider the Poisson equation in 2D as follows:

$$\begin{cases} -\Delta u(x, y) = f(x, y) & \text{in } \Omega \\ u(x, y) = 0 & \text{on } \partial\Omega \end{cases} \quad (13)$$

where $(x, y) \in \Omega = [-1, 1] \otimes [-1, 1]$. In this example, we select the exact solution with multi-scale feature as:

$$u_{\text{exact}}(x, y) = \sin(2\pi x) \sin(4\pi y) + \frac{1}{2} \sin(6\pi x) \sin(8\pi y) \quad (14)$$

The network is trained by minimizing the loss function given below:

$$\begin{aligned} \mathcal{L}(\theta) &= \omega_r \mathcal{L}_r(\theta) + \omega_b \mathcal{L}_b(\theta) \\ &= \frac{\omega_r}{N_r} \sum_{i=1}^{N_r} |\Delta u_\theta(x_r^i, y_r^i) + f(x_r^i, y_r^i)|^2 + \frac{\omega_b}{N_b} \sum_{i=1}^{N_b} |u_\theta(x_b^i, y_b^i)|^2 \end{aligned} \quad (15)$$

Next, we demonstrate the single-resolution training results of two PIML models with the representation model defined by an MLP and a KAN, denoted as SR-PINN and SR-PIKAN. We trained SR-PINN and SR-PIKAN models with comparable numbers

of trainable parameters on this problem. Further details on the network architecture and hyperparameter settings can be found in Appendix A. In this forward problem example, we select $N_b = 800$ sampling points on the boundary and vary the number of residual points as $N_r = 320, 640, 1280, 2560$ and 5120 within the computational domain. In the subsequent discussion, we refer to these as different single-resolution (SR) sampling strategies. As shown in Table 1, for solving physical problems whose solution exhibits multi-scale features such as Equ. 14, low-resolution sampling struggle to achieve satisfactory accuracy. The predicted results with the single-resolution

Table 1: The accuracy of SR-PIKAN and SR-PINN models under different single-resolution settings

Single-resolution setting		$N_r = 320$	$N_r = 640$	$N_r = 1280$	$N_r = 2560$	$N_r = 5120$
L_2 -error	SR-PIKAN	9.195-e01	7.545e-01	4.685e-01	2.048e-01	1.945e-02
	SR-PINN	4.068	2.143	1.990	1.030e-01	3.133e-02

Both SR-PIKAN and SR-PINN models achieve more accurate results as the resolution increases.

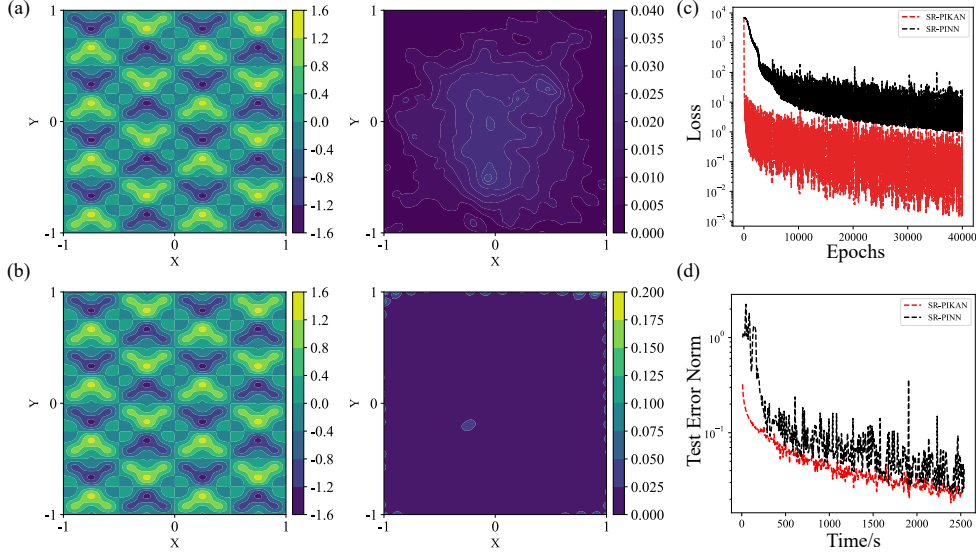


Fig. 4: Results of SR-PIKAN and SR-PINN model trained with the single-resolution setting of $N_r = 5120$: **a** Predicted solution and point-wise error of SR-PIKAN model; **b** Predicted solution and point-wise error of SR-PINN model; **c** Training loss \mathcal{L} over epochs of SR-PIKAN model and SR-PINN model; and **d** Test L_2 -error over training time of SR-PIKAN model and SR-PINN model

setting of $N_r = 5120$ are shown in Fig. 4(a)(b). The results indicate that, with sufficient sampling, both the SR-PINN and SR-PIKAN models can effectively learn problems with multi-scale features. Fig. 4(c)(d) illustrates the evolution of the training loss and L_2 -error for both models throughout the training process. The results also indicate that, after sufficient training, both the PINN and PIKAN models exhibit comparable test accuracy.

Furthermore, we analyzed the training dynamics of SR-PIKAN models at different resolutions from the perspective of IB theory. In the framework of IB theory, a commonly used metric to quantify training dynamics of PIML model is the batch-wise Signal-to-Noise Ratio (SNR), which is defined as:

$$\text{SNR} = \frac{\|\mu\|_2}{\|\sigma\|_2} = \frac{\|\mathbb{E}[\nabla_{\theta}\mathcal{L}_{\mathcal{B}}]\|_2}{\|\text{std}[\nabla_{\theta}\mathcal{L}_{\mathcal{B}}]\|_2} \quad (16)$$

where $\|\mu\|_2$ and $\|\sigma\|_2$ are the L_2 norms of the batch-wise mean and standard deviation (std) of $\nabla_{\theta}\mathcal{L}_{\mathcal{B}}$ for all network parameters. The study in [39] suggests that it is during the total diffusion phase when the neural network achieves optimal convergence. Furthermore, the gradient homogeneity metric, $\text{SRR}_{\mathcal{B}}$, can be used to identify the point at which the model enters the total diffusion phase.

$$\text{SRR}_{\mathcal{B}} = \|\mathbb{E}[\nabla_{\theta}\mathcal{L}_{\mathcal{B}}]\|_2 / \|\sqrt{\mathbb{E}[(\nabla_{\theta}\mathcal{L}_{\mathcal{B}})^2]}\|_2 \quad (17)$$

The SNR is tightly linked to gradient homogeneity metric $\text{SRR}_{\mathcal{B}}$ among samples through the following expression:

$$\text{SNR} = \frac{|\text{SRR}_{\mathcal{B}}|}{\sqrt{1 - \text{SRR}_{\mathcal{B}}^2}}, \quad (18)$$

Further details on the training dynamics can be found in reference [39].

As shown in Fig. 5, all five SR-PIKAN models entered the total diffusion phase after 1000 epochs, during which the gradient homogeneity metric $\text{SRR}_{\mathcal{B}}$ remained at a relatively high level close to 1.0. At this stage, the SNR of each SR-PIKAN model also remained stable, with higher-resolution models demonstrating higher SNR values. The results indicate that for physical fields like Equ. 14, which exhibit multi-scale features, high-resolution sampling can effectively improve the signal-to-noise ratio of the optimization gradients, thereby ensuring solution accuracy.

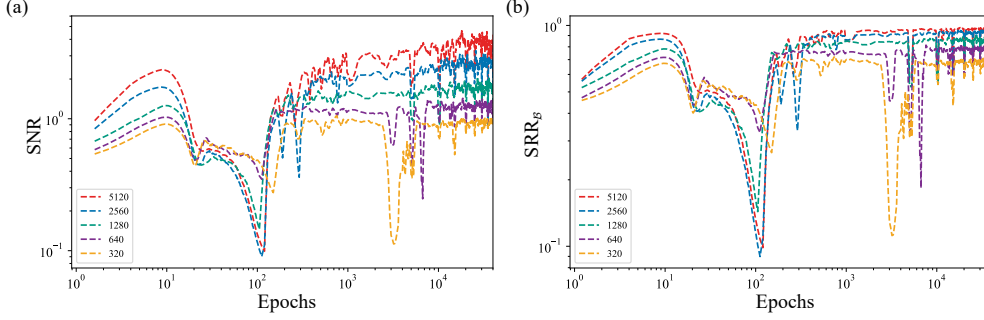


Fig. 5: Training dynamics of SR-PIKAN models trained by different single resolution (full-batch size): **a** Signal-to-Noise Ratio (SNR) of SR-PIKAN models trained by different single resolution; **b** Gradient homogeneity metric SRR_B of SR-PIKAN models trained by different single resolution. All models entered the total diffusion phase after 1000 epochs, during which models trained with higher-resolution sampling exhibited a higher signal-to-noise ratio

3.2 Multi-resolution training strategies

Although the training results for the benchmark problem show that higher-resolution sampling improves both training and test accuracy, it also significantly increases the computational cost. Inspired by multi-grid methods in traditional numerical analysis and the solution of PDEs [40], a multi-resolution (MR) strategy has been introduced for training PIML models. We utilize sampling point sets with multiple resolutions to train the network sequentially or alternately, thereby reducing the training time of the model while ensuring accuracy.

Consider the parameter update operator \mathcal{T} during the gradient descent process, which is expressed as:

$$\theta^{t+1} = \mathcal{T}(\theta^t, \mathcal{G}_n^t) = \theta^t - \eta \cdot \mathcal{G}_n^t \quad (19)$$

where \mathcal{G}_n^t represents the stochastic gradient approximation of the loss function $\mathcal{L}_n(\theta^t)$, which is computed over n sample points. For the single-resolution training strategy described in Section 3.1, the batch size $n = N_{\text{batch}}$ is fixed during the training process. Thus, we have:

$$\mathcal{G}_n^t = \mathcal{G}_{N_{\text{batch}}}^t = \frac{1}{N_{\text{batch}}} \sum_{i=1}^{N_{\text{batch}}} \nabla_{\theta} \mathcal{L}_i(\theta^t) \quad (20)$$

The algorithm for the multi-resolution strategy is shown in Algorithm 1, where the stochastic gradient estimate \mathcal{G}_n^t depends on the training resolution function $N(t)$ at iteration step t . At this point, the stochastic approximation of the gradient takes the form:

$$\mathcal{G}_n^t = \mathcal{G}_{N(t)}^t = \frac{1}{N(t)} \sum_{i=1}^{N(t)} \nabla_{\theta} \mathcal{L}_i(\theta^t) \quad (21)$$

As illustrated in Fig. 6, the MR strategy use both high-resolution and low-resolution sampling batches to train the PIML model in one training process. In Fig.6,

Algorithm 1 Multi-resolution training strategy

Require: Training iterations T , training resolution function $N(t)$

- 1: **Initialization:** Xavier normal scheme [41]: θ^0
 - 2: **for** Training iteration $t = 1, \dots, T$ **do**
 - 3: **Approximate the gradient:** \mathcal{G}_n^t using Equ. 21
 - 4: **Update parameters:** $\theta^{t+1} = \mathcal{T}(\theta^t, \mathcal{G}_n^t)$
 - 5: **end for**
-

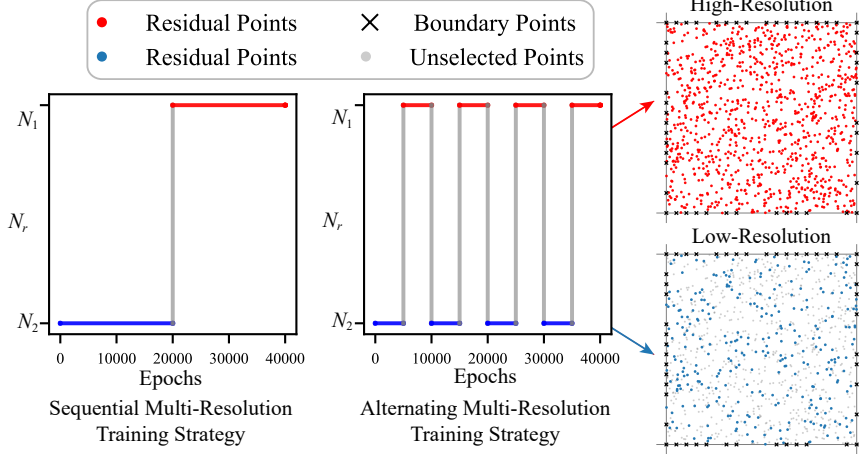


Fig. 6: Multi-resolution training strategies: High-resolution and low-resolution training strategies are defined by randomly selecting residual sampling points with varying batch sizes within the problem domain. The gradient descent process trained with these strategies maintains consistent expected information. Furthermore, sequential or alternate adjustments to the batch sizes of residual points throughout the training process enable the implementation of corresponding multi-resolution training strategies

the red line and sampling points represent the high-resolution case, while the blue line and sampling points represent the low-resolution case. A small, identical set of boundary sampling points (represented by black crosses) is used in both resolution cases. In the sequential multi-resolution strategy, the model is initially trained at a lower resolution for a specific number of epochs and then refined at a higher resolution. In the alternating multi-resolution strategy, the model is trained alternately at two resolutions until completion.

Leveraging the advantages of the KAN network structure in capturing multi-scale features, we propose the PIKAN model with a multi-resolution training strategy, referred to as MR-PIKAN. For forward problems, the network is trained using full-batch sampling points at different resolutions. For inverse problems, however, since a relatively large dataset is required for effective inference, mini-batch sampling at different resolutions is used to train the network. Notably, when the selected low resolution

is sufficiently low, the time and resources required for the forward and backward passes of the model are greatly reduced, thereby greatly improving its training efficiency. In Section 4, we solve a series of forward and inverse problems involving multi-scale features using the proposed MR-PIKAN model, demonstrating its effectiveness and efficiency.

4 Numerical examples

In this section, we demonstrate the performance of the proposed MR-PIKAN model in solving multi-scale forward and inverse problems. For implementation, we develop the PIKAN and PINN frameworks through the PyTorch [42] library in Python. Throughout all benchmarks, we use the hyperbolic tangent as the activation function for the MLP and as the normalizing function for the Chebyshev KAN. The network is initialized using the Xavier normal scheme [41]. All networks are trained using the Adam optimizer [43] with the default setting on a single Nvidia RTX 4070 Ti GPU. In particular, we employ exponential learning rate decay with a decay-rate of 0.9 every 5,000 training iterations. The primary metric used to evaluate the model’s generalization ability is the L_2 -error on the test data set, which is expressed as:

$$L_2\text{-error} = \frac{\|\mathbf{u}_\theta(\mathbf{x}) - \mathbf{u}_{\text{exact}}(\mathbf{x})\|_2}{\|\mathbf{u}_{\text{exact}}(\mathbf{x})\|_2} \quad (22)$$

where $\mathbf{u}_\theta(\mathbf{x})$ and $\mathbf{u}_{\text{exact}}(\mathbf{x})$ represent the model approximation and the exact solution, respectively. The test dataset is relatively dense to provide a more accurate assessment of the model’s generalization ability. More details are provided in Appendix A.

4.1 2D Poisson equation

4.1.1 Multi-resolution training results

First, we solve the problem described in Section 3.1 using MR-PINNs and MR-PIKANs. We select the same PINN and PIKAN models as described in Section 3.1, ensuring that the number of trainable parameters in both models was approximately the same. The MLP in the PINN model has 6 hidden layers, with 72 neurons per layer, activated by a hyperbolic tangent function, resulting in a total of 27,433 trainable parameters. The KAN in the PIKAN model has 2 hidden layers, each with 60 neurons, and utilizes Chebyshev polynomials of up to the 6-th order for activation, with a total of 26,700 trainable parameters. We use the same boundary sampling set of size $N_b = 800$ as described in Section 3.1 to encode the boundary conditions into the loss function. In addition, we set the weight coefficients to $\omega_r = 0.1, \omega_b = 100$ for a more stable training. The size of the test dataset is set to $N_t = 1000 \times 1000$, which is relatively large to better assess the model’s accuracy in capturing multi-scale features of the solution. The initial learning rate of PINNs and PIKANs is set to 1e-3 for this benchmark problem. All results after 40,000 iterations are used for comparison across all examples. The result with $N_r = 5120$ is selected as the training outcome of the model using the single-resolution strategy, hereafter referred to as SR-PINN or SR-PIKAN for further comparison and discussion.

We first sequentially train our model at different resolutions, while keeping all other training parameters consistent with the previous single-resolution settings. As shown by the blue curve in Fig.7(b), the scheme $[[20000, 1280], [20000, 5120]]$ indicates that the model is first trained for 20,000 steps at low resolution ($N_r = 1280$), followed by another 20,000 steps at high-resolution ($N_r = 5120$), completing a total of 40,000 iterations.

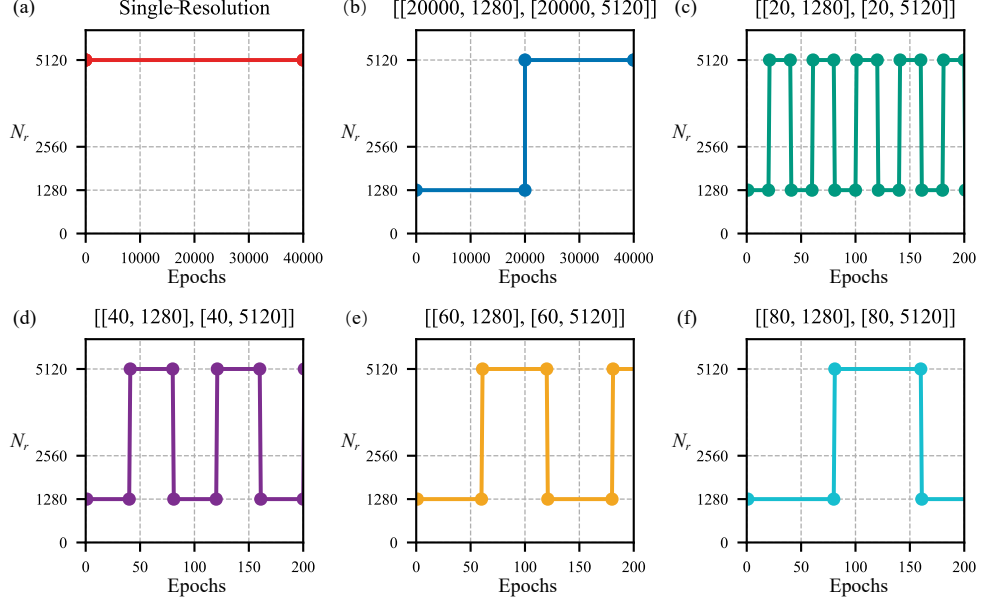


Fig. 7: Training Strategies: **a** Single-resolution training strategy: N_r remains constant throughout the entire training process; **b-f** Multi-resolution training strategies: The notation $[n, N_r]$ indicates a configuration where N_r points are used for n epochs before switching to the next configuration

Fig.8 shows the test L_2 -error norm of the models trained using the multi-resolution training strategy as a function of time. The red dashed lines in Fig. 8 represent the single-resolution training results obtained using a full-batch strategy at a resolution of 5120, which serve as a reference for subsequent multi-resolution training. The results show that models trained with multi-resolution strategies reduce training time while achieving comparable test accuracy, with occasional slight improvements. The blue and magenta lines indicate that the models trained using the two-resolution strategy can reduce the training time by approximately 10%, while the brown line represents the model trained using the three-resolution strategy, where the training time is nearly the same as that of the single-resolution case. As shown in Fig.8(a), the model is first trained at low resolution, quickly reaching an accuracy limit, after which it is unable to learn further until switching to a higher resolution. Therefore, inspired by the multi-grid methods [40] in classical numerical analysis, we can reduce the number of

iterations at each resolution by using an alternating multi-resolution training strategy. Since the model is trained using stochastic gradient descent at various resolutions, the iteration step can be treated as a hyperparameter. Fig.7(c)-(f) illustrate the training strategies of the model when different alternating steps of 20,40,60 and 80 are selected, respectively.

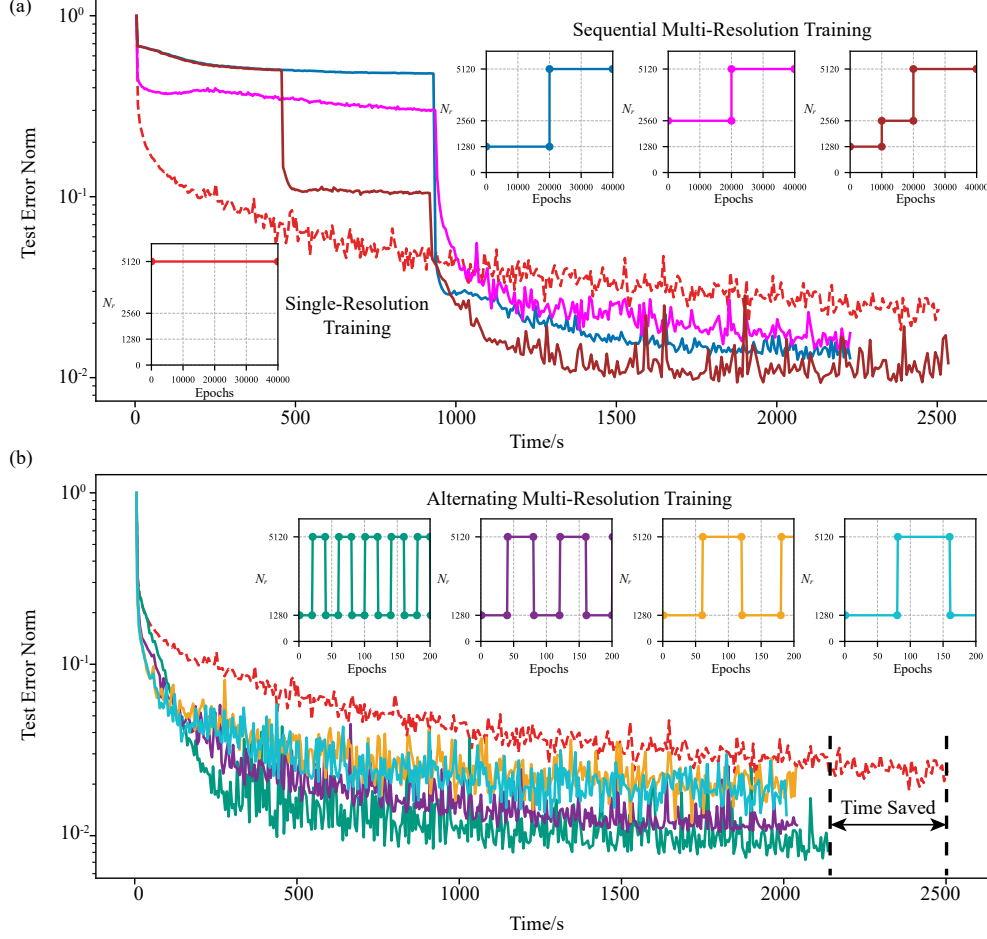


Fig. 8: Convergence process of MR-PIKAN models: **a** Convergence process of sequential multi-resolution PIKAN models: The test errors of the MR-PIKAN models are all lower than the results of the single high-resolution model represented by the red dashed line. During low-resolution training, a convergence plateau is clearly observed, where the test error cannot further decrease until it switches to a higher resolution; **b** Convergence process of alternating multi-resolution PIKAN models: The MR-PIKAN model achieves lower test errors compared to the SR-PIKAN model, while significantly reducing training time

Fig.8(b) shows the test error of the models trained using the alternating multi-resolution training strategy with different step sizes. The results indicate that all models trained using the alternating multi-resolution strategy save approximately one-sixth of the training time compared to the model trained at a single high-resolution, while also achieving improved test accuracy compared to the single-resolution case. The reduction in total training time is mainly attributed to the faster forward and backward passes at lower resolutions. Therefore, when the resolution increases to the point where the hardware can no longer support full-batch training, the alternating multi-resolution training strategy still offers potential for further improvement in training speed. The above results indicate that using the alternating multi-resolution training strategy can effectively accelerate the training of the PIKAN model. In addition, the alternating training strategy performs better than the sequential training strategy, and smaller iteration intervals appear to be more efficient.

4.1.2 Training results of MR-PINNs and comparison across different models

Furthermore, we applied the same alternating multi-resolution training strategy to two types of PINN models, the vanilla PINN models and the Fourier-Feature-enhanced PINN models. The test error convergence and SNR during the training process for MR-PIKAN and the above two models are shown in Fig.9. The results in Fig.9(a)(b) indicate that MR-PIKANs significantly reduce training time compared to SR-PIKAN. Furthermore, the training of the PIKAN models exhibits three typical phases: fitting, diffusion, and total diffusion. The results in Fig.9(c)(d) indicate that the Fourier-feature-enhanced PINN models trained with the multi-resolution strategy achieve accuracy comparable to that of single-resolution training. The training dynamics during the convergence process are similar to those of the PIKAN models. However, no significant time savings are observed with the multi-resolution models. As shown in Fig.9(e)(f), the vanilla PINN model, with a comparable number of trainable parameters, fails to achieve the same order of test accuracy as the previous two models on this problem. These vanilla PINN models exhibit a high SNR during the fitting phase in the first 100 epochs. However, they primarily capture lower-frequency components and become trapped in local minima. In the total diffusion phase, the SNR of the PINN models does not surpass that of the initial fitting phase, primarily due to the spectral bias of the MLP architecture. In summary, this comparison highlights the superior performance of MR-PIKAN in both accuracy and efficiency. Moving forward, we employ the MR-PIKAN model to tackle challenging inverse problems with multi-scale features.

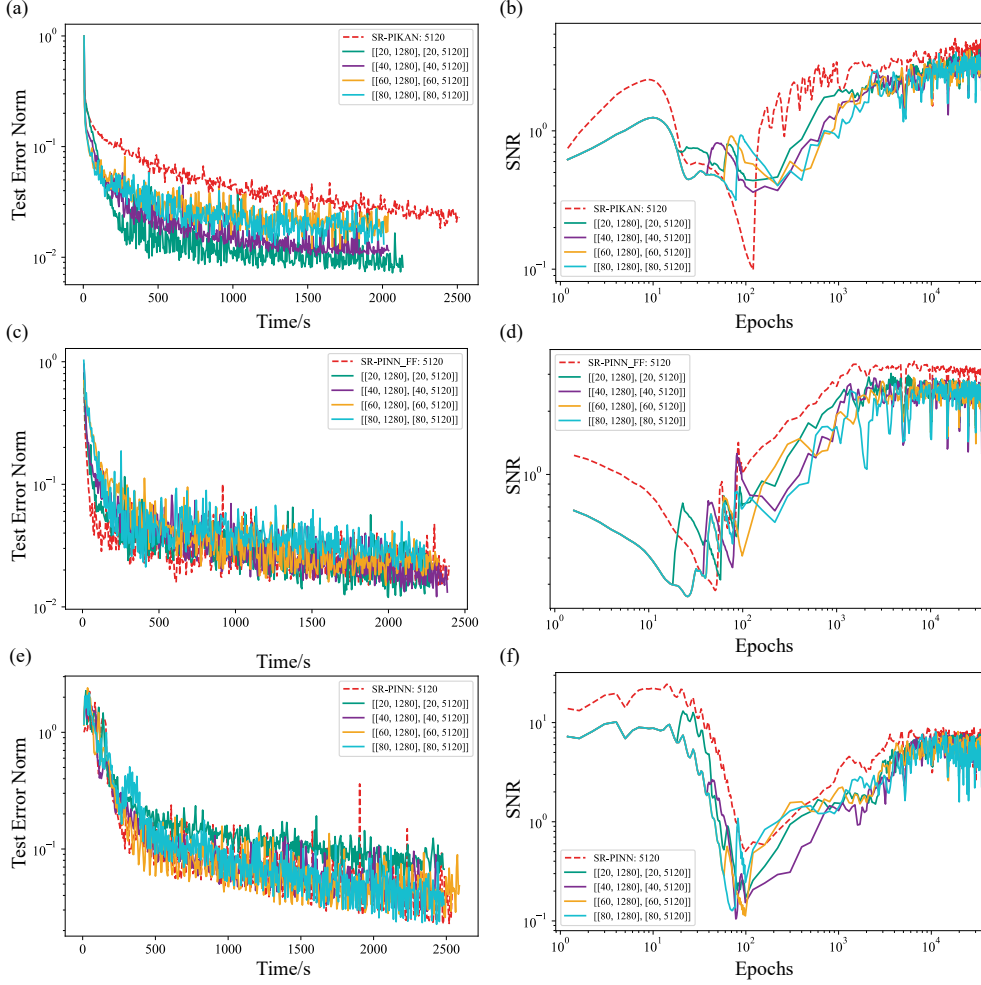


Fig. 9: Training dynamics of MR-PIKANs, MR-PINNs and MR-PINNs with Fourier-feature embedding: **a** Convergence process of MR-PIKAN models: A significant reduction in training time compared to the single-resolution model can be observed; **b** Training dynamics of MR-PIKAN models: Three typical phases can be observed: fitting, diffusion and total diffusion; **c** Convergence process of MR-PINN models with Fourier-feature embedding: The results obtained using single-resolution and multi-resolution training strategies for this type of model are similar in terms of both accuracy and training time; **d** Training dynamics of MR-PINN models with Fourier-feature embedding: The models exhibit results similar to those for PIKAN models; **e** Convergence process of MR-PINN models: The vanilla PINN models, with a comparable number of trainable parameters, fails to achieve the same order of test accuracy as the previous two models on this problem; and **f** Training dynamics of MR-PINN models: Vanilla PINN models exhibit a high SNR during the fitting phase; however, in the final total diffusion phase, the SNR fails to reach the values achieved during the initial phase

4.2 Reaction-diffusion dynamics in a two-dimensional Gray-Scott model

This example aims to highlight the performance of the proposed MR-PIKAN model to handle inverse problems. Consider a two-dimensional Gray-Scott model [44] that describes a chemical reaction between two substances U and V , both of which diffuse over time. The Gray-Scott system is defined by two coupled equations that describe the behavior of two reacting substances:

$$\begin{aligned} u_t &= \varepsilon_1 \Delta u + b(1 - u) - uv^2 \\ v_t &= \varepsilon_2 \Delta v - dv + uv^2 \end{aligned} \quad (23)$$

where Δ is the Laplacian, and u, v represent the concentrations of two reacting substances U, V , both of which diffuse over time at the diffusion rates ε_1 and ε_2 . In this inverse problem, we aim to infer the parameters ε_1 and ε_2 of this time-dependent PDE based on several observed snapshots of the concentration fields u and v .

Referring to [11], we generate a dataset containing a numerical solution of the two-dimensional Gray-Scott equations with 40,000 spatial points and 401 temporal snapshots. Specifically, we take $b = 0.04$, $d = 0.1$, $\varepsilon_1 = 2e - 5$, $\varepsilon_2 = 1e - 5$ and start from an initial condition

$$\begin{aligned} u(x, y, 0) &= 1 - \exp\left(-80(x + 0.05)^2 + (y + 0.02)^2\right) \quad (x, y) \in [-1, 1] \times [-1, 1] \\ v(x, y, 0) &= \exp\left(-80(x - 0.05)^2 + (y - 0.02)^2\right) \quad (x, y) \in [-1, 1] \times [-1, 1] \end{aligned} \quad (24)$$

and integrate the equations up to the final time $t = 4000$. Synthetic training data for this example are generated using the Chebfun package [45] with a spectral Fourier discretization and a fourth-order stiff time-stepping scheme [46] with time-step size of 0.5. We collect the data points $\{(t^i, x^i, y^i), (\bar{u}^i, \bar{v}^i)\}_{i=1}^N$ from time $t = 3900$ to $t = 4000$ (a total of 10 snapshots) as our training dataset. Fig.10(a)(d) display a characteristic "fingerprint," illustrating a solution with intricate spatial structures and rich frequency components.

To invert the unknown diffusion rates ε_1 and ε_2 , we employ the proposed MR-PIKAN model to predict the concentration fields u and v , simultaneously treating the unknown coefficients $\varepsilon_1, \varepsilon_2$ as trainable parameters. To better handle the non-trivial frequency features in the concentration fields, we use Chebyshev polynomials of up to the 15-th order as activation functions while retaining the network architecture with two hidden layers, each containing 50 neurons. The corresponding loss function

is given by

$$\begin{aligned}
\mathcal{L}(\boldsymbol{\theta}) &= \omega_{r^u} \mathcal{L}_{r^u}(\boldsymbol{\theta}) + \omega_{r^v} \mathcal{L}_{r^v}(\boldsymbol{\theta}) + \omega_{d^u} \mathcal{L}_{d^u}(\boldsymbol{\theta}) + \omega_{d^v} \mathcal{L}_{d^v}(\boldsymbol{\theta}) \\
&= \frac{1}{N_r} \sum_{i=1}^{N_r} |\mathcal{D}^u[u_{\boldsymbol{\theta}}](x_r^i, y_r^i, t_r^i)|^2 + \frac{1}{N_r} \sum_{i=1}^{N_r} |\mathcal{D}^v[v_{\boldsymbol{\theta}}](x_r^i, y_r^i, t_r^i)|^2 \\
&\quad + \frac{1}{N_d} \sum_{i=1}^{N_d} |u_{\boldsymbol{\theta}}(x_d^i, y_d^i, t_d^i) - \bar{u}(x_d^i, y_d^i, t_d^i)|^2 + \frac{1}{N_d} \sum_{i=1}^{N_d} |v_{\boldsymbol{\theta}}(x_d^i, y_d^i, t_d^i) - \bar{v}(x_d^i, y_d^i, t_d^i)|^2
\end{aligned} \tag{25}$$

where (x_r^i, y_r^i, t_r^i) and (x_d^i, y_d^i, t_d^i) represent the physics-informed sampling points and the observed data sampling points, respectively. \bar{u} and \bar{v} denote the observed values of the concentration fields. For the single-resolution case, we select mini-batch sizes of $N_d = 1,000$ and $N_r = 5,000$, where all data points are randomly sampled from the observed dataset, and all residual points are randomly sampled within the computational domain. In particular, since the diffusion rates are strictly positive and generally very small, we refer to [11] and parameterize $\varepsilon_1, \varepsilon_2$ by exponential functions, that is, $\varepsilon_i = e^{\alpha_i}$ for $i = 1, 2$, where α_1, α_2 are trainable parameters initialized by -10. All models are trained by minimizing the above loss function via 120,000 iterations of gradient descent.

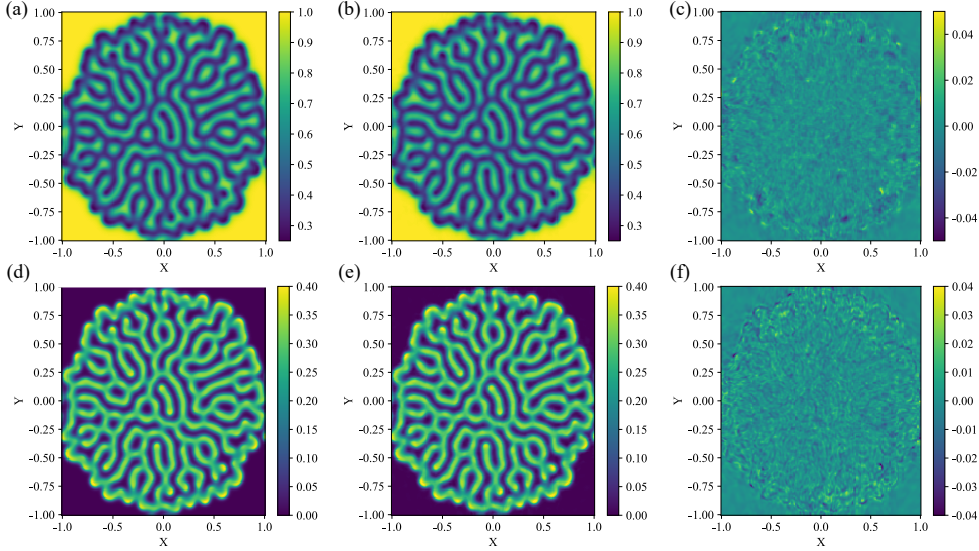


Fig. 10: Field results learned by MR-PIKAN model of the 2D Gray-Scott model at $t = 4000$: **a** Reference concentration solution u ; **b** Predicted concentration solution u ; **c** Point-wise solution error Δu ; **d** Reference concentration solution v ; **e** Predicted concentration solution v ; and **f** Point-wise solution error Δv

The predicted solutions and point-wise errors of the concentration fields u and v at $t = 4000$ obtained using the MR-PIKAN model are illustrated in Fig.10. The results demonstrate excellent agreement between the predicted values and the reference numerical approximation. In addition, Fig.11 illustrates the evolution of the inferred diffusion rates obtained using the SR-PIKAN and MR-PIKAN models. The final inferred diffusion coefficients are presented in Table.2, showing that both the SR-PIKAN and MR-PIKAN models exhibit good agreement with the exact values. The inversion errors of all PIKAN models are within 2%, while the MR-PIKAN models reduce the training time by 20% compared to the SR-PIKAN model.

Table 2: Comparison of the inversion errors and training times of the SR-PIKAN and MR-PIKAN models for the inverse 2D Gray-Scott problem

Model	Resolution	ε_1		ε_2		Training Time/s
		Inferred	Relative	Inferred	Relative	
		Value	Error	Value	Error	
SR-PIKAN	5000	1.977e-5	1.15%	9.832e-6	1.68%	38026
	[10, 5000] , [10, 1000]	1.977e-5	1.15%	9.830e-6	1.70%	29299
MR-PIKAN	[20, 5000] , [20, 1000]	1.976e-5	1.20%	9.912e-6	1.88%	29347
	[40, 5000] , [40, 1000]	1.979e-5	1.05%	9.833e-6	1.67%	28959
	[80, 5000] , [80, 1000]	1.978e-5	1.10%	9.834e-6	1.66%	28554

Exact parameter values: $\varepsilon_1=2e-5$, $\varepsilon_2=1e-5$.

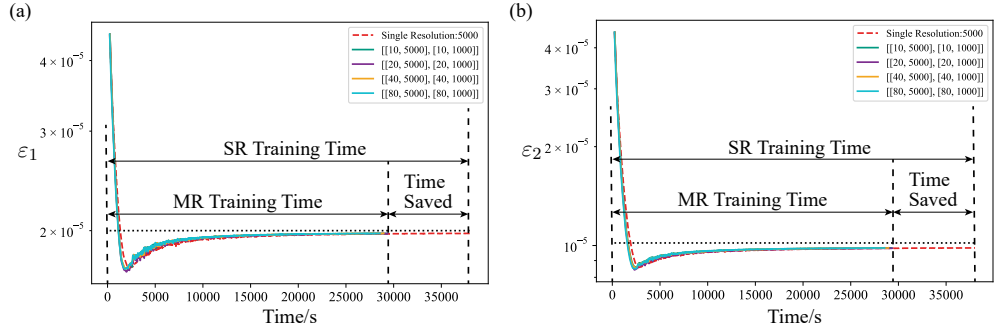


Fig. 11: Convergence process of unknown diffusion rates for MR-PIKAN models: Both the SR-PIKAN and MR-PIKAN models accurately invert the diffusion coefficients, with test errors within 2%. The MR-PIKAN models achieve the same level of accuracy as the SR-PIKAN model while reducing training time by 20%. **a** Convergence process of diffusion rate ε_1 ; **b** Convergence process of diffusion rate ε_2

4.3 Hidden elasticity of two-phase random material

The last example further evaluates the performance of the MR-PIKAN model in an inverse problem involving the reconstruction of parameter fields with complex multi-scale features. Two-phase random materials (TRMs), such as polyurethane [47], dual-phase (DP) steels [48] and nanocomposites [49], are an important class of materials in advanced material research whose properties are closely related to their microstructures. In this example, we consider a two-phase square plate with a length of 2 mm. The microstructure of this TRM plate, as shown in Fig.12(a), is constructed by the random field level-cutting method [50]. Assuming that the interfaces between

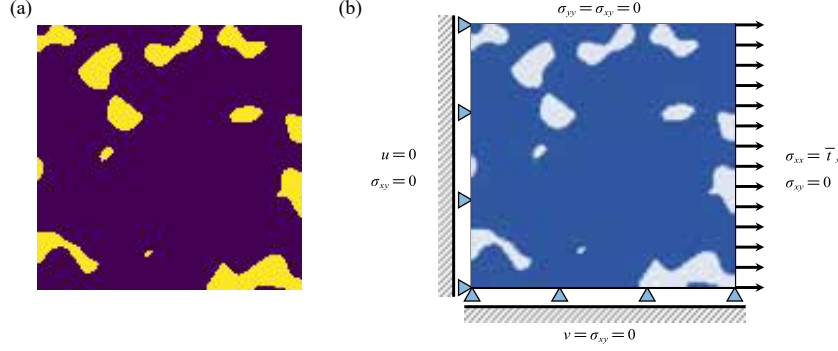


Fig. 12: Microstructure of TRMs and boundary conditions of the problem: **a** Microstructure of TRMs; **b** Boundary conditions set up

the two phases are perfectly bonded and each phase is an isotropic elastic material, the governing equations can be expressed in the following form:

$$\begin{aligned}\sigma_{ij,j} &= 0 \\ \sigma_{ij} &= \lambda \delta_{ij} \varepsilon_{kk} + 2\mu \varepsilon_{ij} \\ \varepsilon_{ij} &= \frac{1}{2} (u_{i,j} + u_{j,i})\end{aligned}\tag{26}$$

where σ_{ij} and ε_{ij} are components of the Cauchy stress tensor and components of the infinitesimal strain tensor, respectively, with ε_{ij} derived from the displacements u_i . λ and μ , known as Lamé constants, can be related to the elastic modulus and Poisson's ratio through the following equations:

$$\begin{aligned}E &= \frac{\mu(3\lambda + 2\mu)}{(\lambda + \mu)} \\ \nu &= \frac{\lambda}{2(\lambda + \mu)}\end{aligned}\tag{27}$$

In engineering practice, for a given two-phase material plate subjected to known surface force boundary conditions, global strain field data can be obtained non-destructively through various imaging techniques [51, 52]. Therefore, in this inverse problem, we aim to infer the elastic parameter fields $E(x, y)$ and $\nu(x, y)$ of this two-phase material plate based on observed strain field $\{(\bar{\varepsilon}_{xx}^i, \bar{\varepsilon}_{yy}^i, \bar{\varepsilon}_{xy}^i)\}_{i=1}^{N_\varepsilon}$ and the known surface force boundary conditions $\{(\bar{\sigma}_{xx}^i, \bar{\sigma}_{yy}^i)\}_{i=1}^{N_\sigma}$.

The FEM method was used to generate the numerical solution with 128×128 elements. The boundary conditions are illustrated in Fig.12(b), where the right side of the plate is subjected to a surface traction of $\bar{\sigma}_{xx} = 80\text{MPa}$. Fig.14(a) and (d) shows the exact elastic modulus field and Poisson's ratio field of the plate. We collect the strain field $\{(\bar{\varepsilon}_{xx}^i, \bar{\varepsilon}_{yy}^i, \bar{\varepsilon}_{xy}^i)\}_{i=1}^{N_\varepsilon}$ and the stress components $\{(\bar{\sigma}_{xx}^i, \bar{\sigma}_{yy}^i)\}_{i=1}^{N_\sigma}$ on the boundaries as the training data set. The stress fields obtained from the reference solution using FEM are shown in Fig.13.

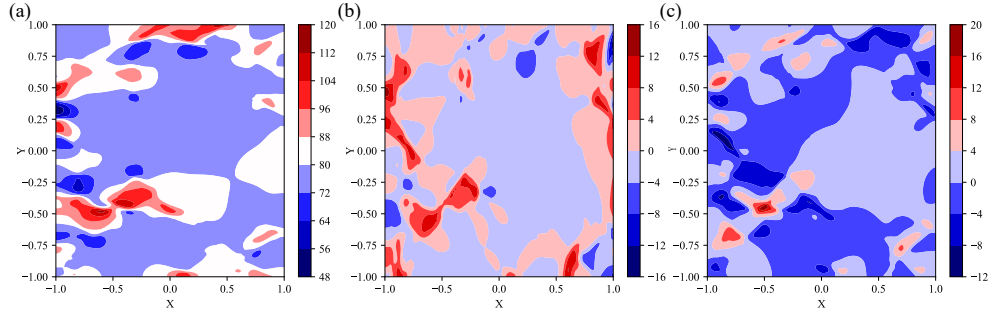


Fig. 13: Reference stress fields of TRM plates: **a** Stress field σ_{xx} ; **b** Stress field σ_{yy} ; **c** Stress field σ_{xy} ; The reference stress components $\{(\sigma_{xx}^i, \sigma_{yy}^i)\}_{i=1}^{N_\sigma}$ at the boundaries are consistent with the known surface force boundary conditions $\{(\bar{\sigma}_{xx}^i, \bar{\sigma}_{yy}^i)\}_{i=1}^{N_\sigma}$. Together with the strain fields $\{(\bar{\varepsilon}_{xx}^i, \bar{\varepsilon}_{yy}^i, \bar{\varepsilon}_{xy}^i)\}_{i=1}^{N_\varepsilon}$ within the domain, these constitute the observed training dataset

To invert the parameter field of this two-phase material, we utilize the proposed MR-PIKAN framework to predict the stress field and material parameter field of the aforementioned plate. To better handle the non-trivial frequency features of two-phase materials, we employ Chebyshev polynomials of up to the 15-th order as activation functions, while maintaining a network architecture with three hidden layers, each consisting of 60 neurons. To effectively represent the stress field and material parameter field with multiple components using one single neural network, we modify the final layer of the standard KAN structure into a learnable linear layer, thereby accelerating the model's convergence. To address the challenge of learning two types of field variables with significant amplitude differences, we introduced some scaling factors and derive their equivalent dimensionless governing equations, as detailed in [53].

The corresponding loss function is given by:

$$\begin{aligned}
\mathcal{L}(\boldsymbol{\theta}) &= \omega_{\sigma_{xx}} \mathcal{L}_{\sigma_{xx}} + \omega_{\sigma_{yy}} \mathcal{L}_{\sigma_{yy}} + \omega_{c_{xx}} \mathcal{L}_{c_{xx}} + \omega_{c_{yy}} \mathcal{L}_{c_{yy}} + \omega_{c_{xy}} \mathcal{L}_{c_{xy}} + \omega_{r_x} \mathcal{L}_{r_x} + \omega_{r_y} \mathcal{L}_{r_y} \\
&= \frac{\omega_{\sigma_{xx}}}{N_\sigma} \sum_{i=1}^{N_\sigma} |\sigma_{xx}^\theta - \bar{\sigma}_{xx}|^2 + \frac{\omega_{\sigma_{yy}}}{N_\sigma} \sum_{i=1}^{N_\sigma} |\sigma_{yy}^\theta - \bar{\sigma}_{yy}|^2 + \frac{\omega_{c_{xy}}}{N_c} \sum_{i=1}^{N_c} |2\mu \bar{\varepsilon}_{xy} - \sigma_{xy}^\theta|^2 \\
&\quad + \frac{\omega_{c_{xx}}}{N_c} \sum_{i=1}^{N_c} |(\lambda + 2\mu) \bar{\varepsilon}_{xx} + \lambda \bar{\varepsilon}_{yy} - \sigma_{xx}^\theta|^2 + \frac{\omega_{c_{yy}}}{N_c} \sum_{i=1}^{N_c} |(\lambda + 2\mu) \bar{\varepsilon}_{yy} + \lambda \bar{\varepsilon}_{xx} - \sigma_{yy}^\theta|^2 \\
&\quad + \frac{\omega_{r_x}}{N_r} \sum_{i=1}^{N_r} |\sigma_{xx,x}^\theta + \sigma_{xy,y}^\theta|^2 + \frac{\omega_{r_y}}{N_r} \sum_{i=1}^{N_r} |\sigma_{yx,x}^\theta + \sigma_{yy,y}^\theta|^2
\end{aligned} \tag{28}$$

where variables with the superscript $\boldsymbol{\theta}$ represent the results approximated by the neural network. $\bar{\varepsilon}_{xx}, \bar{\varepsilon}_{yy}, \bar{\varepsilon}_{xy}$ denote the observed value of the strain field and $\bar{\sigma}_{xx}, \bar{\sigma}_{yy}$ denote the known boundary conditions. To avoid training pathologies and better balance the seven loss terms, we employ the adaptive weighting method [34] proposed by Wang et al. All training is done for 400,000 iterations, and the initial learning rate is set as $1e-4$. For the single-resolution case, we choose the mini-batch size $N_\sigma = N_c = N_r = 2000$. Moreover, we train the same PIKAN model with alternating multi-resolution strategy. The predicted solution and point-wise error of the material property fields learned by MR-PIKAN model are shown in Fig. 14. The results demonstrate a strong alignment between the predictions and the ground truth of the parameter field.

Fig. 15 shows the L_2 error of the models trained using the multi-resolution training strategy with different step sizes. The results show that the proposed MR-PIKAN model requires less than half the time of the single high-resolution model for the same number of iterations. Moreover, the time taken by the MR-PIKAN model to achieve an acceptable accuracy (within 1%) for the inferred elastic parameter fields is over 30% less than that required by the SR-PIKAN model.

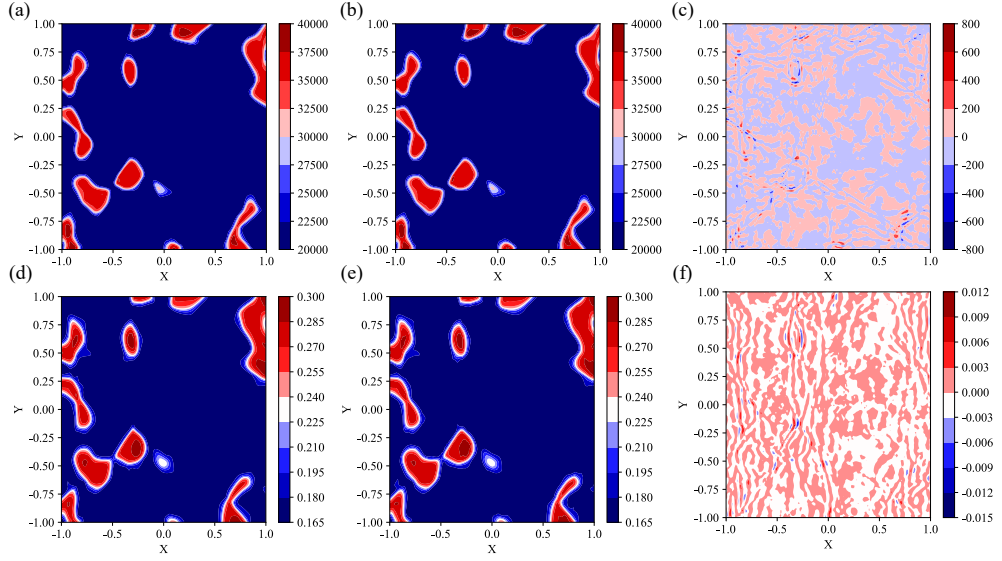


Fig. 14: Material parameter field results learned by MR-PIKAN model of TRMs: The test errors of parameter field obtained by the PIKAN models are all below 5%. **a** Reference Young's Modulus E ; **b** Predicted Young's Modulus E ; **c** Point-wise solution error of Young's Modulus ΔE ; **d** Reference Poisson's Ratio ν ; **e** Predicted Poisson's Ratio ν ; and **f** Point-wise solution error of Poisson's Ratio $\Delta \nu$

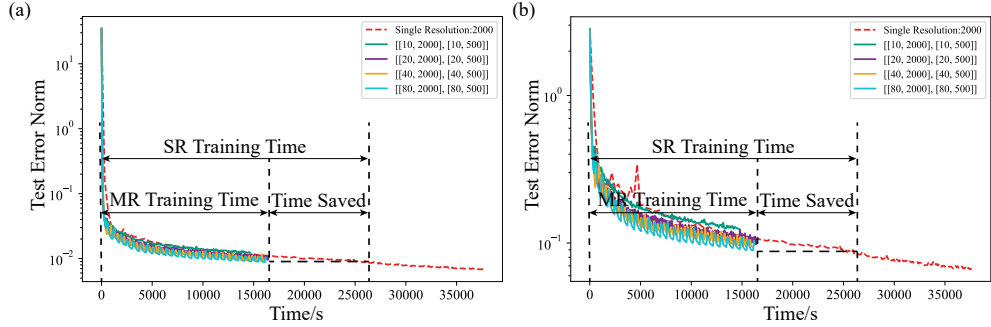


Fig. 15: The convergence process of the SR-PIKAN model and the MR-PIKAN model achieving comparable error norms: It can be observed that the MR-PIKAN model significantly reduces the training time required to achieve acceptable training accuracy compared to the SR-PIKAN model. **a** The convergence process of material parameter field; **b** The convergence process of stress field

5 Discussion

In this work, we propose a simple yet effective multi-resolution training-enhanced PIKAN framework, referred to as MR-PIKAN, which trains the model sequentially or alternately at different resolutions. We validate the effectiveness and efficiency of the MR-PIKAN model in solving forward and inverse problems with complex multi-scale features. We begin by solving a 2D forward Poisson problem using different single-resolution settings and analyze their training dynamics. The results empirically demonstrate that higher-resolution sampling is crucial for accurately capturing multi-scale features. Furthermore, inspired by the classical multi-grid method, we propose a multi-resolution training strategy to reduce the overall training time required for accurately capturing multi-scale features. The implementation of the proposed MR-PIKAN model is straightforward, as the interactions between resolutions are weak.

We evaluate the proposed MR-PIKAN model through three numerical examples, demonstrating its accuracy and efficiency. For forward problems, which typically require a large number of full-batch sampling points, the alternating multi-resolution strategy significantly reduces computational time. By leveraging the advantages of KAN in learning high-frequency functions, the model better captures the multi-scale features of physical systems. For inverse problems, where mini-batch training is commonly used, the multi-resolution training strategy enhances training efficiency while maintaining comparable test accuracy. Therefore, MR-PIKAN effectively accelerates the solution of forward and inverse problems involving multi-scale physical features, without sacrificing accuracy compared to the high-resolution SR-PIKAN model. Additionally, the multi-resolution training strategy proposed in this paper focuses on training with random sampling points at different resolutions, and can be combined with existing adaptive sampling algorithms to further enhance the modeling of multi-scale physical problems.

Statements and Declarations

Acknowledgements. This work was supported by the National Natural Science Foundation of China (under grant numbers 92270115, 12071301) and Shanghai Municipal Science and Technology Commission (Grant No. 20JC1412500) to Ling Guo; the National Natural Science Foundation of China (Grant No. 52478198) and Shanghai Municipal Science and Technology Commission (Grant No. 24510711500) to Xiaodan Ren.

Competing Interests. The authors declare that they have no known competing financial interests or personal relationships that could have appeared to influence the work reported in this paper.

Appendix A Implementation details of PIKAN and PINN models

The network parameters are initialized using Xavier normal distribution [31]. The rest of the case-specific information are tabulated in Table.A1-Table.A3.

Implementation details: Forward 2D Poisson Problem			
Network approximation		$u_{\theta}(x, y)$	
Network Detail	Architecture	KAN	MLP
	Number of hidden layers	2	6
	Neurons per layer	60	72
	Activation function	Chebyshev polynomials	tanh
		$T_0(x) \cdots T_6(x)$	
	Number of parameters	26700	27433
Initial learning rate		1e-3	
Full-batch size of collocation points		SR:5120	MR:1280, 2560, 5120
Full-batch size of boundary condition points		800	
Number of epochs		40000	
Decay rate		0.9	
Decay step		5000	
Global weight of residual term		0.1	
Global weight of boundary condition term		100	

Table A1: Implementation details of forward Poisson case

References

- [1] Dissanayake, M.W.M.G., Phan-Thien, N.: Neural-network-based approximations for solving partial differential equations. Communications in Numerical Methods in Engineering **10**(3), 195–201 (1994) <https://doi.org/10.1002/cnm.1640100303>
- [2] Lagaris, I.E., Likas, A., Fotiadis, D.I.: Artificial neural networks for solving ordinary and partial differential equations. IEEE Transactions on Neural Networks **9**(5), 987–1000 (1998) <https://doi.org/10.1109/72.712178>
- [3] Weinan, E., Yu, B.: The deep ritz method: A deep learning-based numerical algorithm for solving variational problems. Communications in Mathematics and Statistics **6**(1), 1–12 (2018) <https://doi.org/10.1007/s40304-018-0127-z>
- [4] Karniadakis, G.E., Kevrekidis, I.G., Lu, L., Perdikaris, P., Wang, S., Yang, L.: Physics-informed machine learning. Nature Reviews Physics **3**(6), 422–440 (2021) <https://doi.org/10.1038/s42254-021-00314-5>
- [5] Raissi, M., Perdikaris, P., Karniadakis, G.E.: Physics informed deep learning (part i): Data-driven solutions of nonlinear partial differential equations. arXiv preprint arXiv:1711.10561 (2017)
- [6] Raissi, M., Perdikaris, P., Karniadakis, G.E.: Physics informed deep learning (part ii): Data-driven discovery of nonlinear partial differential equations. arXiv preprint arXiv:1711.10566 (2017)

Implementation details: Inverse Gray-Scott Model		
Network approximation	$[u_{\theta}(x, y, t), v_{\theta}(x, y, t)]$	
Network architecture	KAN	
Number of hidden layers	2	
Neurons per layer	50	
Activation function	Chebyshev polynomials: $T_0(x) \cdots T_{15}(x)$	
Number of parameters	44200	
Initial learning rate	1e-3	
Number of data points	400000	
Mini-batch size of collocation points	SR: 5000	MR: 1000, 5000
Mini-batch size of data points	SR: 1000	MR: 1000, 1000
Number of epochs	120000	
Decay rate	0.9	
Decay step	5000	
Global weight of each loss term	1.0	

Table A2: Implementation details of inverse Gray-Scott model

- [7] Kharazmi, E., Zhang, Z., Karniadakis, G.E.: Variational physics-informed neural networks for solving partial differential equations. arXiv preprint arXiv:1912.00873 (2019)
- [8] Samaniego, E., Anitescu, C., Goswami, S., Nguyen-Thanh, V.M., Guo, H., Hamdia, K., Zhuang, X., Rabczuk, T.: An energy approach to the solution of pdes via ml. Computer Methods in Applied Mechanics and Engineering **362**, 112790 (2020) <https://doi.org/10.1016/j.cma.2019.112790>
- [9] Chen, T.: Approximations of continuous functionals by neural networks with application to dynamic systems. IEEE Transactions on Neural Networks **4**(6), 910–918 (1993) <https://doi.org/10.1109/72.286886>
- [10] Rahaman, N., Baratin, A., Arpit, D., Draxler, F., Lin, M., Hamprecht, F., Bengio, Y., Courville, A.: On the spectral bias of neural networks. In: Proceedings of the 36th International Conference on Machine Learning, vol. 97, pp. 5301–5310. PMLR, (2019)
- [11] Wang, S., Wang, H., Perdikaris, P.: On the eigenvector bias of fourier feature networks. Computer Methods in Applied Mechanics and Engineering **384**, 113938 (2021) <https://doi.org/10.1016/j.cma.2021.113938>
- [12] Jagtap, A.D., Kawaguchi, K., Karniadakis, G.E.: Adaptive activation functions accelerate convergence in deep and physics-informed neural networks. Journal of Computational Physics **404**, 109136 (2020) <https://doi.org/10.1016/j.jcp.2019.109136>

Implementation details: Hidden elasticity of TRMs		
Network approximation	$[\sigma_{xx}^\theta(x, y), \sigma_{yy}^\theta(x, y), \sigma_{xy}^\theta(x, y)]$ and $[\lambda^\theta(x, y), \mu^\theta(x, y)]$	
Network architecture	KAN	
Number of hidden KAN layers	3	
Neurons per layer	60	
Activation function	Chebyshev polynomials: $T_0(x) \cdots T_{15}(x)$	
Number of parameters	117303 and 117242	
Initial learning rate	1e-4	
Number of data points	16384	
Mini-batch size of collocation points	SR: 2000	MR: 500, 2000
Mini-batch size of data points	SR: 2000	MR: 500, 2000
Number of epochs	4000	
Number of iterations per epoch	100	
Decay rate	0.9	
Decay step	5000	
Initial global weight of each loss term	1.0	

Table A3: Implementation details of hidden elasticity case

- [13] Li, X.-A., Xu, Z.-Q.J., Zhang, L.: A multi-scale dnn algorithm for nonlinear elliptic equations with multiple scales. arXiv preprint arXiv:2009.14597 (2020)
- [14] Huang, J., You, R., Zhou, T.: Frequency-adaptive multi-scale deep neural networks. arXiv preprint arXiv:2410.00053 (2024)
- [15] Liu, Z., Wang, Y., Vaidya, S., Ruehle, F., Halverson, J., Soljačić, M., Hou, T.Y., Tegmark, M.: Kan: Kolmogorov-arnold networks. arXiv preprint arXiv:2404.19756 (2024)
- [16] Liu, Z., Ma, P., Wang, Y., Matusik, W., Tegmark, M.: Kan 2.0: Kolmogorov-arnold networks meet science. arXiv preprint arXiv:2408.10205 (2024)
- [17] Shukla, K., Toscano, J.D., Wang, Z., Zou, Z., Karniadakis, G.E.: A comprehensive and fair comparison between mlp and kan representations for differential equations and operator networks. Computer Methods in Applied Mechanics and Engineering **431**, 117290 (2024) <https://doi.org/10.1016/j.cma.2024.117290>
- [18] Sidharth, S., Keerthana, A., Gokul, R., Anas, K.: Chebyshev polynomial-based kolmogorov-arnold networks: An efficient architecture for nonlinear function approximation. arXiv preprint arXiv:2405.07200 (2024)
- [19] Li, Z.: Kolmogorov-arnold networks are radial basis function networks. arXiv preprint arXiv:2405.06721 (2024)
- [20] Bozorgasl, Z., Chen, H.: Wav-kan: Wavelet kolmogorov-arnold networks. arXiv

preprint arXiv:2405.12832 (2024)

- [21] Wang, Y., Sun, J., Bai, J., Anitescu, C., Eshaghi, M.S., Zhuang, X., Rabczuk, T., Liu, Y.: Kolmogorov arnold informed neural network: A physics-informed deep learning framework for solving pdes based on kolmogorov arnold networks. arXiv preprint arXiv:2406.11045 (2024)
- [22] Lu, L., Meng, X., Mao, Z., Karniadakis, G.E.: Deepxde: A deep learning library for solving differential equations. *SIAM Review* **63**(1), 208–228 (2021) <https://doi.org/10.1137/19M1274067>
- [23] Wu, C., Zhu, M., Tan, Q., Kartha, Y., Lu, L.: A comprehensive study of non-adaptive and residual-based adaptive sampling for physics-informed neural networks. *Computer Methods in Applied Mechanics and Engineering* **403**, 115671 (2023) <https://doi.org/10.1016/j.cma.2022.115671>
- [24] Mao, Z., Meng, X.: Physics-informed neural networks with residual/gradient-based adaptive sampling methods for solving partial differential equations with sharp solutions. *Applied Mathematics and Mechanics* **44**(7), 1069–1084 (2023) <https://doi.org/10.1007/s10483-023-2994-7>
- [25] Gao, Z., Yan, L., Zhou, T.: Failure-informed adaptive sampling for pinns. *SIAM Journal on Scientific Computing* **45**(4), 1971–1994 (2023) <https://doi.org/10.1137/22M1527763>
- [26] Rigas, S., Papachristou, M., Papadopoulos, T., Anagnostopoulos, F., Alexandridis, G.: Adaptive training of grid-dependent physics-informed kolmogorov-arnold networks. arXiv preprint arXiv:2407.17611 (2024)
- [27] Nabian, M.A., Gladstone, R.J., Meidani, H.: Efficient training of physics-informed neural networks via importance sampling. *Computer-Aided Civil and Infrastructure Engineering* **36**(8), 962–977 (2021) <https://doi.org/10.1111/mice.12685>
- [28] Tang, K., Wan, X., Yang, C.: Das-pinns: A deep adaptive sampling method for solving high-dimensional partial differential equations. *Journal of Computational Physics* **476**, 111868 (2023) <https://doi.org/10.1016/j.jcp.2022.111868>
- [29] Aldirany, Z., Cottureau, R., Laforest, M., Prudhomme, S.: Multi-level neural networks for accurate solutions of boundary-value problems. *Computer Methods in Applied Mechanics and Engineering* **419**, 116666 (2024) <https://doi.org/10.1016/j.cma.2023.116666>
- [30] Wang, Y., Lai, C.-Y.: Multi-stage neural networks: Function approximator of machine precision. *Journal of Computational Physics* **504**, 112865 (2024) <https://doi.org/10.1016/j.jcp.2024.112865>
- [31] Song, S., Mukerji, T., Zhang, D.: Physics-informed multi-grid neural operator:

- Theory and an application to porous flow simulation. *Journal of Computational Physics* **520**, 113438 (2025) <https://doi.org/10.1016/j.jcp.2024.113438>
- [32] Wu, C.-Y., Girshick, R., He, K., Feichtenhofer, C., Krahenbuhl, P.: A multigrid method for efficiently training video models. In: *Proceedings of the IEEE/CVF Conference on Computer Vision and Pattern Recognition (CVPR)*, pp. 153–162 (2020). <https://doi.org/10.1109/CVPR42600.2020.00023>
 - [33] Lin, L., Wang, X., Qi, Z., Shan, Y.: Accelerating the training of video super-resolution models. In: *Proceedings of the AAAI Conference on Artificial Intelligence*, vol. 37(2), pp. 1595–1603 (2023)
 - [34] Wang, S., Teng, Y., Perdikaris, P.: Understanding and mitigating gradient pathologies in pinns. *SIAM Journal on Scientific Computing* **43**(5), 3055–3081 (2021) <https://doi.org/10.1137/20M1318043>
 - [35] Wang, S., Yu, X., Perdikaris, P.: When and why pinns fail to train: A neural tangent kernel perspective. *Journal of Computational Physics* **449** (2022) <https://doi.org/10.1016/j.jcp.2021.110768>
 - [36] McClenny, L.D., Braga-Neto, U.M.: Self-adaptive physics-informed neural networks. *Journal of Computational Physics* **474**, 111722 (2023) <https://doi.org/10.1016/j.jcp.2022.111722>
 - [37] Anagnostopoulos, S.J., Toscano, J.D., Stergiopoulos, N., Karniadakis, G.E.: Residual-based attention in physics-informed neural networks. *Computer Methods in Applied Mechanics and Engineering* **421**, 116805 (2024) <https://doi.org/10.1016/j.cma.2024.116805>
 - [38] Kolmogorov, A.N.: On the representation of continuous functions of many variables by superposition of continuous functions of one variable and addition. In: *Doklady Akademii Nauk SSSR*, vol. 114(5), pp. 953–956 (1957). Russian Academy of Sciences
 - [39] Anagnostopoulos, S.J., Toscano, J.D., Stergiopoulos, N., Karniadakis, G.E.: Learning in pinns: Phase transition, total diffusion, and generalization. *arXiv preprint arXiv:2403.18494* (2024)
 - [40] Hackbusch, W.: *Multi-Grid Methods and Applications*. Springer Series in Computational Mathematics, vol. 4. Springer, (1985). <https://doi.org/10.1007/978-3-662-02427-0>
 - [41] Glorot, X., Bengio, Y.: Understanding the difficulty of training deep feedforward neural networks. In: Teh, Y.W., Titterton, M. (eds.) *Proceedings of the Thirteenth International Conference on Artificial Intelligence and Statistics. Proceedings of Machine Learning Research*, vol. 9, pp. 249–256. PMLR, (2010)

- [42] Paszke, A., Gross, S., Massa, F., Lerer, A., Bradbury, J., Chanan, G., Killeen, T., Lin, Z., Gimelshein, N., Antiga, L., Desmaison, A., Kopf, A., Yang, E., DeVito, Z., Raison, M., Tejani, A., Chilamkurthy, S., Steiner, B., Fang, L., Bai, J., Chintala, S.: Pytorch: An imperative style, high-performance deep learning library. In: *Advances in Neural Information Processing Systems*, vol. 32. Curran Associates, Inc., (2019)
- [43] Kingma, D.P., Ba, J.: Adam: A method for stochastic optimization. In: *International Conference on Learning Representations (ICLR2015)*. Ithaca, NY, (2015)
- [44] Gray, P., Scott, S.K.: *Chemical Oscillations and Instabilities: Non-linear Chemical Kinetics*. Oxford University Press, (1990)
- [45] Driscoll, T.A., Hale, N., Trefethen, L.N.: *Chebfun guide*. Pafnuty Publications, Oxford (2014)
- [46] Cox, S.M., Matthews, P.C.: Exponential time differencing for stiff systems. *Journal of Computational Physics* **176**(2), 430–455 (2002)
- [47] Liu, B., Wang, Y., Rabczuk, T., Olofsson, T., Lu, W.: Multi-scale modeling in thermal conductivity of polyurethane incorporated with phase change materials using physics-informed neural networks. *Renewable Energy* **220**, 119565 (2024) <https://doi.org/10.1016/j.renene.2023.119565>
- [48] Tasan, C.C., Diehl, M., Yan, D., Bechtold, M., Roters, F., Schemmann, L., Zheng, C., Peranio, N., Ponge, D., Koyama, M.: An overview of dual-phase steels: advances in microstructure-oriented processing and micromechanically guided design. *Annual Review of Materials Research* **45**(1), 391–431 (2015) <https://doi.org/10.1146/annurev-matsci-070214-021103>
- [49] Iyer, A., Zhang, Y., Prasad, A., Tao, S., Wang, Y., Schadler, L., Brinson, L.C., Chen, W.: Data-centric mixed-variable bayesian optimization for materials design. In: *International Design Engineering Technical Conferences and Computers and Information in Engineering Conference*, vol. 2A, pp. 02–03066 (2019)
- [50] Ren, X., Lyu, X.: Mixed form based physics-informed neural networks for performance evaluation of two-phase random materials. *Engineering Applications of Artificial Intelligence* **127** (2024) <https://doi.org/10.1016/j.engappai.2023.107250>
- [51] Blaber, J., Adair, B., Antoniou, A.: Ncorr: Open-source 2d digital image correlation matlab software. *Experimental Mechanics* **55**(6), 1105–1122 (2015) <https://doi.org/10.1007/s11340-015-0009-1>
- [52] Chen, C.-T., Gu, G.X.: Learning hidden elasticity with deep neural networks. *Proceedings of the National Academy of Sciences* **118**(31), 2102721118 (2021)

<https://doi.org/10.1073/pnas.2102721118>

- [53] Langtangen, H.P., Pedersen, G.K.: Scaling of Differential Equations. Springer, (2016)